Article:
Wookey, J., Kendall, J.M. and Barruol, G. (2002) Mid-mantle deformation inferred from seismic anisotropy. Nature, 415 (6873). pp. 777-780. ISSN 0028-0836

https://doi.org/10.1038/415777a

changed uniformly by +5 K, −10 K or −20 K. Additional experiments, not presented here, demonstrated insensitivity of the simulated heat fluxes to changes in surface fluxes of heat, moisture and momentum, or in scale-selective dissipation.

Except as noted below, all quantities used to create Figs 1–3 are zonal means, averaged over the mid-latitude region defined as 1,000–200 mbar, 28°–68° latitude, for each hemisphere. The results were found to be insensitive to variations in the definition of the mid-latitude region. In particular, this height is sufficient to include essentially the whole troposphere and all the eddy activity. It should be noted that the average meridional temperature gradient is closely constrained by the fixed surface temperatures, and could be replaced by the surface temperature gradient in the calculations with only a modest loss in accuracy. The diabatic forcing term q includes both the radiative heating averaged over the mid-latitude region and the surface fluxes of sensible heat, although the contribution of surface fluxes turns out to be small. The height scales H and H_s, used to calculate the radius of deformation L_D, and the Charney length scale L_γ, were taken to be constant at 8 km as they did not vary substantially in any of the experiments. In calculating L_γ, the vertical averages were weighted[13] by a factor $e^{-z/D}$, where $D = H_s/(0.48 + 1.48\gamma)$. The latitude of the zonal wind maximum, which did not vary substantially between experiments, was used to calculate f and β. The size of the baroclinic zone, L_{zone}, was defined as the distance between the two latitudes where the strength of the vertically averaged zonal-mean zonal wind first drops to half of its maximum value. In all calculations the correlation coefficient k was given a constant value of 0.25, while the utilization coefficient e was given a constant value of 0.75.

Received 1 November; accepted 18 December 2001.

1. Pierrehumbert, R. T. & Swanson, K. L. Baroclinic instability. *Annu. Rev. Fluid Mech.* **27,** 419–467 (1995).
2. Held, I. M. The macroturbulence of the troposphere. *Tellus A* **51,** 59–70 (1999).
3. Green, J. S. Transfer properties of the large scale eddies and the general circulation of the atmosphere. *Q. J. R. Meteorol. Soc.* **96,** 157–185 (1970).
4. Stone, P. H. A simplified radiative-dynamical model for the static stability of rotating atmospheres. *J. Atmos. Sci.* **29,** 405–418 (1972).
5. Branscome, L. E. A parameterization of transient eddy heat flux on a beta plane. *J. Atmos. Sci.* **41,** 2508–2521 (1983).
6. Held, I. M. & Larichev, V. D. A scaling theory for horizontally homogeneous, baroclinically unstable flow on a beta plane. *J. Atmos. Sci.* **53,** 946–952 (1996).
7. Haine, T. W. N. & Marshall, J. Gravitational, symmetric and baroclinic instability of the ocean mixed layer. *J. Phys. Oceanogr.* **28,** 634–658 (1998).
8. Barry, L., Thuburn, J. & Craig, G. C. GCM tests of some possible dynamical constraints on the mid-latitude atmosphere: The v'–T' correlation, PV homogenisation and the dividing isentrope. *Q. J. R. Meteorol. Soc.* (submitted).
9. Pavan, V. & Held, I. M. The diffusive approximation for eddy fluxes in baroclinically unstable jets. *J. Atmos. Sci.* **53,** 1262–1272 (1996).
10. Eady, E. T. Long waves & cyclone waves. *Tellus* **1,** 33–52 (1949).
11. Charney, J. G. The dynamics of long waves in a baroclinic westerly current. *J. Meteorol.* **4,** 135–162 (1947).
12. Held, I. M. The vertical scale of an unstable baroclinic wave and its importance for eddy heat flux parameterisation. *J. Atmos. Sci.* **35,** 572–576 (1978).
13. Stone, P. H. & Yao, M.-S. Development of a 2-dimensional zonally averaged statistical-dynamic model. 3. The parameterisation of eddy fluxes of heat and moisture. *J. Clim.* **3,** 726–740 (1990).
14. Charney, J. G. Geostrophic turbulence. *J. Atmos. Sci.* **28,** 1087–1095 (1971).
15. Salmon, R. *Lectures on Geophysical Fluid Dynamics* (Oxford Univ. Press, Oxford, 1998).
16. Larichev, V. D. & Held, I. M. Eddy amplitudes and fluxes in a homogeneous model of fully developed baroclinic instability. *J. Phys. Oceanogr.* **25,** 2285–2297 (1995).
17. Rhines, P. B. Waves and turbulence on a beta-plane. *J. Fluid. Mech.* **69,** 417–443 (1975).
18. James, I. N. *Introduction to Circulating Atmospheres* (Cambridge Univ. Press, Cambridge, 1994).
19. Golitsyn, G. S. A similarity approach to the general circulation of planetary atmospheres. *Icarus* **13,** 1–24 (1970).
20. Stone, P. H. & Miller, D. A. Empirical relations between seasonal changes in meridional temperature gradients and meridional fluxes of heat. *J. Atmos. Sci.* **37,** 1708–1721 (1980).
21. Vallis, G. K. Numerical studies of eddy transport properties in eddy-resolving and parameterised models. *Q. J. R. Meteorol. Soc.* **114,** 183–204 (1988).
22. Stone, P. H. & Branscome, L. Diabatically forced, nearly inviscid eddy regimes. *J. Atmos. Sci.* **49,** 355–367 (1992).
23. Panetta, R. L. Zonal jets in wide baroclinically unstable regions: persistence and scale selection. *J. Atmos. Sci.* **29,** 2073–2106 (1993).
24. James, I. N. Two parameterisations of the temperature flux due to baroclinic waves. *Q. J. R. Meteorol. Soc.* **123,** 1–16 (1997).
25. Visbeck, M., Marshall, J. & Haine, T. Specification of eddy transfer coefficients in coarse resolution ocean circulation models. *J. Phys. Oceanogr.* **27,** 381–402 (1997).
26. Forster, P. M. de F., Blackburn, M., Glover, R. & Shine, K. P. An examination of climate sensitivity for idealised climate change experiments in an intermediate general circulation model. *Clim. Dyn.* **16,** 833–849 (2000).
27. Barry, L. *Predicting Eddy Heat Transport in the Troposphere* Thesis, Univ. Reading (2000).
28. Boer, G. & Denis, B. Numerical convergence of the dynamics of a GCM. *Clim. Dyn.* **13,** 359–374 (1997).

Competing interests statement

The authors declare that they have no competing financial interests.

Correspondence and requests for materials should be addressed to G.C.C. (e-mail: G.C.Craig@Reading.ac.uk).

Mid-mantle deformation inferred from seismic anisotropy

James Wookey*, J.-Michael Kendall* & Guilhem Barruol†

* *School of Earth Sciences, University of Leeds, Woodhouse Lane, Leeds LS2 9JT, UK*
† *CNRS, Université Montpellier, 34095 Montpellier, Cedex 05, France*

With time, convective processes in the Earth's mantle will tend to align crystals, grains and inclusions. This mantle fabric is detectable seismologically, as it produces an anisotropy in material properties—in particular, a directional dependence in seismic-wave velocity. This alignment is enhanced at the boundaries of the mantle where there are rapid changes in the direction and magnitude of mantle flow[1], and therefore most observations of anisotropy are confined to the uppermost mantle or lithosphere[2,3] and the lowermost-mantle analogue of the lithosphere, the D″ region[4]. Here we present evidence from shear-wave splitting measurements for mid-mantle anisotropy in the vicinity of the 660-km discontinuity, the boundary between the upper and lower mantle. Deep-focus earthquakes in the Tonga–Kermadec and New Hebrides subduction zones recorded at Australian seismograph stations record some of the largest values of shear-wave splitting hitherto reported. The results suggest that, at least locally, there may exist a mid-mantle boundary layer, which could indicate the impediment of flow between the upper and lower mantle in this region.

Seismic anisotropy in the upper 200 km of the Earth's mantle is primarily attributed to the preferred alignment of olivine crystals which have deformed by dislocation creep[5]. The origin of anisotropy at greater depths is more speculative, but there is evidence for anisotropy in the transition zone in some regions[6–8], but not in others[9,10]. In an effort to reconcile discrepancies in global velocity models derived from body-wave travel times and normal-mode observations, Montagner and Kennett[11] allowed both anisotropy and attenuation in a joint inversion of these data sets. Their final model shows significant levels of anisotropy in the uppermost and lowermost mantle, but also in the vicinity of the 660-km discontinuity (hereafter referred to as the '660'). This motivated an investigation of mid-mantle anisotropy on a regional scale. Here we investigate shear-wave splitting in deep-focus events that image a region below the Australian plate (Fig. 1).

Stations in Australia are ideal for investigating near-source anisotropy, as studies have shown that they exhibit very little, if any, receiver-side shear-wave splitting[12–14] (see Supplementary Information for a summary of observations). For example, 52 SKS measurements with good azimuthal coverage at the station CAN (see Fig. 1 for location) show that shear waves that are travelling nearly vertically are not split while crossing the Australian lithosphere beneath this station[12]. In contrast, we find that deep-focus events from the Tonga–Kermadec and New Hebrides subduction zones show very large degrees of shear-wave splitting at this and four other Australian stations (Fig. 2), suggesting anisotropy deeper in the mantle, away from the receiver.

We made splitting measurements from 92 events, at epicentral distances of 24° to 59° from the Australian stations, using the method of ref. 15, which estimates the time separation between the fast and slow shear wave, δt, and the polarization of the fast shear wave at the receiver, ϕ. This method attempts to remove the anisotropy-induced splitting by minimizing the shear-wave signal in the direction perpendicular to the polarization direction of the shear wave before entering the anisotropic region[16]. A grid search over δt and ϕ is used to estimate the splitting parameters, and a statistical F-test is used to assess errors. The correction for splitting should produce a linear S-wave particle motion, thus providing a further measure of confidence in the results. Of 164 splitting measurements, 66 gave very convincing results—that is, the error in δt is less than 0.5 s, and the error in ϕ is less than 10°. In an effort to isolate mid-mantle anisotropy, we further restricted our study to the 30 events deeper than 300 km which gave 35 high-quality splitting estimates (see Supplementary Information; 75% of the events are greater than 500 km deep). The magnitude of splitting for these events ranges from 0.6 s to 7.1 s. Many measurements show splitting in excess of 4 s (Fig. 2), and suggest either very high degrees of localized anisotropy or wave propagation through a more moderately anisotropic region of large extent. It should be noted that the maximum free-surface incidence angle for our data set is less than 32°, thus avoiding the effects of waveform distortion due to free- and near-surface coupling.

The azimuthal ray coverage at the midpoint between source and receiver spans a 60° region centred around 260°. The polarization of the fast shear wave is roughly aligned with the transverse component, but there is some scatter in this (back-azimuth $-\phi$ = 108° ± 31°). Although the azimuthal ray coverage is not complete, the results suggest a transversely isotropic symmetry with the symmetry axis in the vertical plane, perpendicular to the ray direction. For horizontally travelling rays, this would imply a horizontally polarized fast shear wave (that is, SH leads SV).

To help guide interpretations of these observations, we model wave propagation through an anisotropic slab region using ray theory[17]. The linear slab extends to a depth of 660 km and has a 60° dip angle. Anisotropy in the deeper parts of the slab may be due to the alignment of metastable olivine[18], or the preferred alignment of akimotoite, a polymorph of enstatite, which may exist under slab pressures and temperatures[19]. Alternatively, transition-zone deformation above the slab may align its dominant minerals, wadsleyite and ringwoodite. Finally, anisotropy below the '660' may be due to the alignment of lower-mantle minerals such as perovskite, periclase and/or stishovite, all of which are highly anisotropic[20]. Perovskite is the most likely candidate as it constitutes nearly 80% of the minerals in this region, but an alignment mechanism for perovskite is still uncertain[21,22]. Both experimental measurements[23] and first-principles calculations[24,25] suggest that perovskite is only mildly orthorhombic in symmetry and can be well approximated as being transversely isotropic. Unfortunately, these elastic constants predict that for horizontally travelling waves, vertically polarized shear waves are faster than horizontally polarized shear waves. Alternatively, the anisotropy may not be due to crystal alignment, but rather to the horizontal alignment of tabular inclusions, as has been suggested for the lowermost mantle[4].

Figure 2 compares predicted splitting for a variety of models and the observed splitting values. Consistent with the observations, the anisotropy is constrained to have a fast horizontally polarized shear wave. Very high degrees of anisotropy, distributed throughout the slab, are required to explain the observations with slab anisotropy. It is virtually impossible to explain 6 seconds of splitting in the deepest events (>600 km) with slab anisotropy. An absence of slab anisotropy is further suggested from an analysis of depth-dependent splitting for vertically travelling shear waves beneath Tonga, which shows no evidence of azimuthal anisotropy below 400 km (ref. 10). A lack of SKS splitting does not necessarily mean that the uppermost mantle beneath the receivers is isotropic. Transverse isotropy anywhere in the mantle will not split vertically polarized SKS phases, but will split an arbitrarily polarized S wave. However, Fig. 2 shows that the splitting for an uppermost mantle with 4% anisotropy[26] cannot explain the results. Similarly, they cannot be explained with anisotropy confined to the transition zone, a conclusion reinforced by the fact that ringwoodite, the dominant mineral between depths of 520 and 660 km, is thought to be only very mildly anisotropic[20]. It is difficult to explain the splitting with combinations of transverse isotropy in the uppermost mantle and in transition-zone regions. A problem with models where anisotropy is confined to the upper mantle is that they predict very large amounts of splitting at near offsets and little at large offsets, an effect not seen in the data. Such anisotropy may contribute to the splitting, but cannot explain the observations.

The modelling shows that moderate amounts of anisotropy in the lower mantle generate large amounts of splitting owing to long horizontal ray-paths below the '660' at these epicentral distances. Assuming that the anisotropy is confined to a layer 100 km below the '660', the average anisotropy magnitude is 3.0%. However, Fig. 1 shows that there is spatial variation in this estimate, with the largest

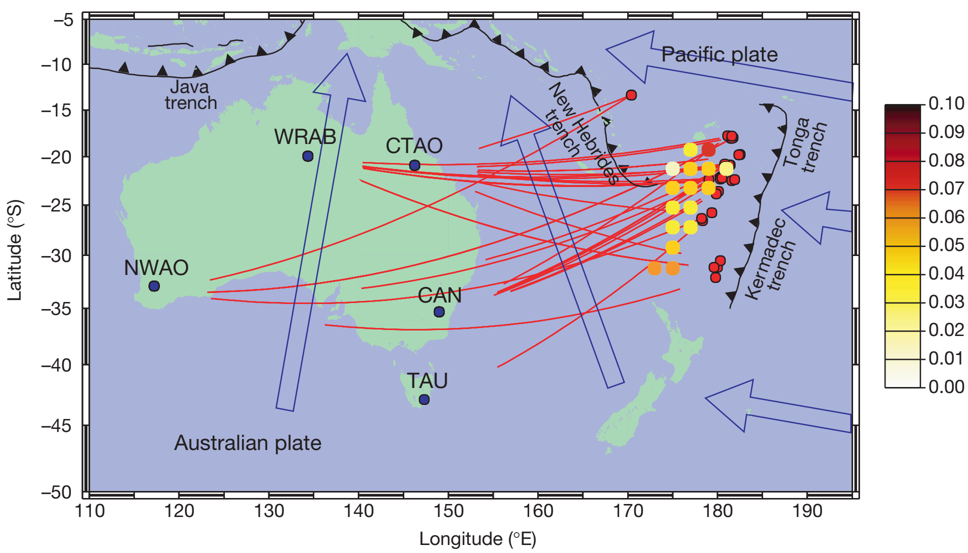

Figure 1 Event–station combinations used to study mid-mantle anisotropy. Small red dots show events; blue dots show stations; red swaths show corresponding lower-mantle ray-paths. Subduction zones and directions of absolute plate motion are also indicated. The larger circles near the events are colour-coded averages (minimum 3 hits) over a 2° radius surface region of the anisotropy magnitude required to explain observed shear-wave splitting, plotted at the point a ray enters the lower mantle. This is calculated assuming that the anisotropy is distributed throughout a 100-km-thick layer just below the 660-km discontinuity (the '660'). Colour scale bar to the right indicates the magnitude of the anisotropy (fractional difference between slow and fast shear wave velocity).

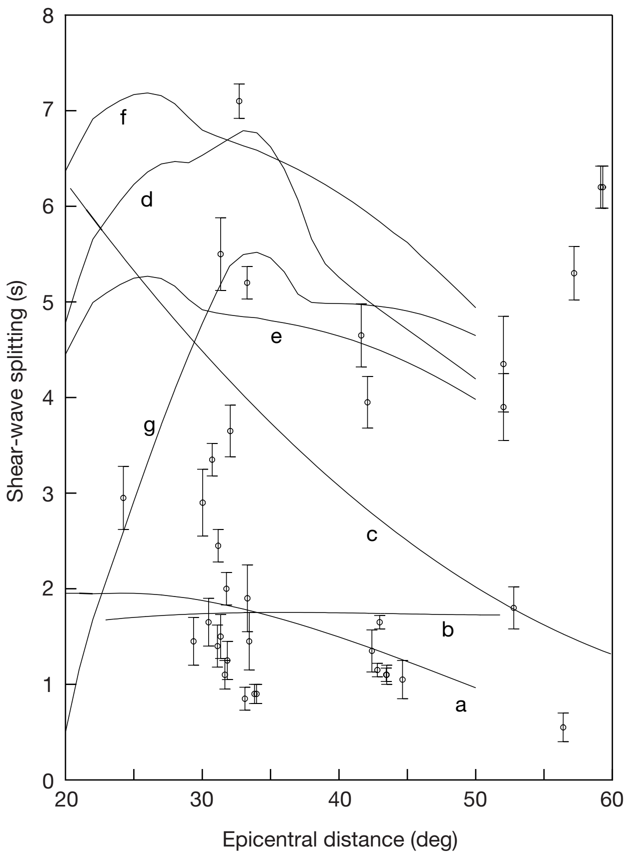

Figure 2 Shear-wave splitting versus epicentral distance. Circles with error bars show observations and estimated uncertainty. Solid lines show predictions for a 500-km-deep source in models with a fast horizontally polarized shear wave: trace a, 4% transverse-isotropy in the uppermost 210 km of upper mantle; b, 5% anisotropy in a subducted slab that extends to a depth of 660 km; c, 5% anisotropy confined to a 100-km-thick layer immediately beneath the '660'; d, anisotropy that grades from 3% to 1% between the '660' and 900 km; e, 2% anisotropy in 100-km-thick layers above and below the '660', and 1% anisotropy in a layer between 760 km and 900 km; f, 4% anisotropy in the uppermost 210 km, 2% anisotropy in 100-km-thick layers above and below the '660', and 1% anisotropy in a layer between 760 km and 900 km; g, anisotropy that grades from 2.5% to 1.5% in a layer between 760 km and 900 km. Although there is some ambiguity as to the best model, only models with anisotropy in the lower mantle can explain the large splitting observations.

magnitude of anisotropy lying in the northernmost and southernmost regions. This north–south variation is also seen in the raw splitting values, with a large range of splitting near 20° S (see Supplementary Information). Alternatively, the magnitude of the anisotropy may grade into the isotropic mantle over a few hundred kilometres, thereby requiring even less anisotropy. Figure 2 also shows that it is difficult accurately to constrain the anisotropy to a layer immediately beneath the '660'. In fact, anisotropy between depths of 760 km and 900 km explains the trend in the large residuals quite well. In summary, the modelling shows that there must be anisotropy below the '660', but not deeper than 900 km, and there may or may not be a contribution from anisotropy above the '660'.

Although there must be anisotropy in the lower mantle, it may still be slab related. Numerical simulations have shown that large deviatoric stresses are transmitted into the lower mantle when a rigid slab encounters an increase in viscosity at the '660' (ref. 27). Large stresses increase the likelihood of dislocation creep mechanisms being active. With time, the associated strains will induce alignment in a broad region below the slab. Perovskite may therefore align with a rotated symmetry axis conformal to the shape of this region. Aligned perovskite rotated more than 30° predicts SH waves faster than SV wave for horizontally travelling S waves.

Another possibility is that the anisotropy is associated with slab material which has broadened and pooled at the '660', before sinking into the deeper mantle. This may be slab material horizontally emplaced on the '660', but our modelling shows that a significant portion of the slab must be well below a depth of 660 km. An alternative is the idea that eclogitic oceanic crust delaminates from the slab, residing in a 'megalith' just below the '660' (ref. 28). This thin crustal layer may thicken appreciably with long-lived subduction into the high-viscosity lower mantle[29]. Furthermore, it has been argued that basalt may be near its solidus in the uppermost and lowermost parts of the lower mantle[30]. Thus the anisotropy may be due to the preferred alignment of melt inclusions (a mechanism which generates anisotropy very effectively[4]), which results from shear deformation at the '660'.

Supporting evidence for the anisotropy being confined to a broad region around the base of the slab comes from recent tomographic images for both P and S waves for the Tonga–Kermadec region[31]. This raises the question of to what degree tomographic images obtained assuming isotropy are influenced by anisotropy. Tomographic images also show along-strike variations in the Tonga–

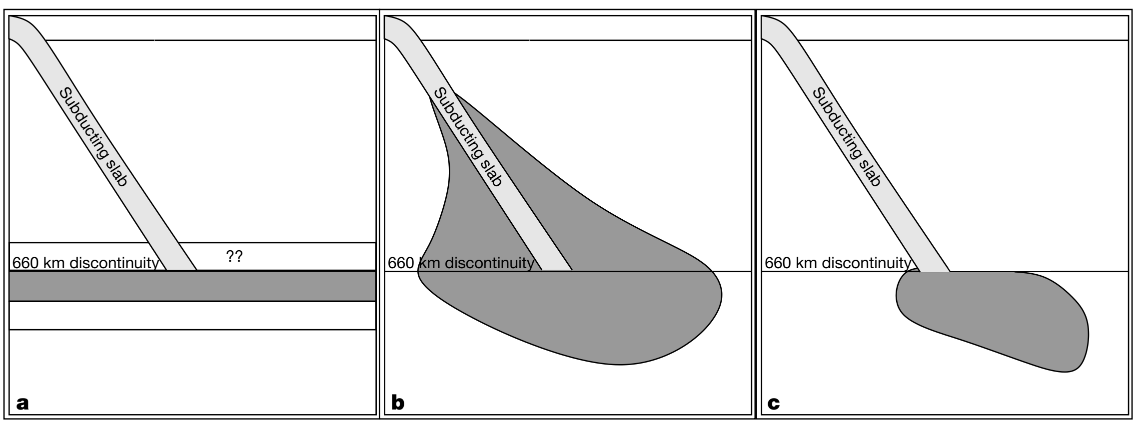

Figure 3 Three models for anisotropy below the 660-km discontinuity. **a**, An anisotropic mid-mantle boundary layer near the '660' that may or may not be a global feature of this boundary. Our results suggest that the magnitude of anisotropy in such a layer must vary laterally quite significantly. **b**, Slab forces on the surrounding mantle lead to strain-induced anisotropy. **c**, Anisotropy associated with slab material pooling in the lower mantle.

Kermadec slab morphology, with a significant change in slab dip near 25° (ref. 32). We note that it is from this region that we observe the smallest amounts of splitting.

Although the precise origin of the anisotropy is not clear at present, our observations and linked modelling show evidence for anisotropy in the uppermost lower mantle beneath the eastern part of the Australian plate. The anisotropy is probably inhomogeneous, as there appears to be an appreciable north–south variability in its magnitude. There must be large strains in this region, which are probably related to slab interaction with the sharp increase in viscosity at this boundary. Figure 3 summarizes the potential mechanisms that we propose. Our results may help describe to what extent there is an impediment of flow at this boundary between the upper and lower mantle. □

Received 5 September; accepted 31 December 2001.

1. Montagner, J.-P. Where can seismic anisotropy be detected in the Earth's mantle? In boundary layers .... *Pure Appl. Geophys.* **151,** 223–256 (1998).
2. Silver, P. G. Seismic anisotropy beneath the continents: Probing the depths of geology. *Annu. Rev. Earth Planet Sci.* **24,** 385–432 (1996).
3. Savage, M. K. Seismic anisotropy and mantle deformation: What have we learned from shear wave splitting? *Rev. Geophys.* **37,** 65–106 (1999).
4. Kendall, J.-M. & Silver, P. G. in *The Core-Mantle Boundary Region* (eds Gurnis, M., Wysession, M., Knittle, E. & Buffett, B.) 97–118 (Geodynamics series 28, American Geophysical Union, Washington DC, 1998).
5. Karato, S. & Wu, P. Rheology of the upper mantle: A synthesis. *Science* **260,** 771–778 (1993).
6. Vinnik, L. P. & Montagner, J.-P. Shear wave splitting in the mantle Ps phase. *Geophys. Res. Lett.* **23,** 2449–2452 (1996).
7. Vinnik, L. P., Chevrot, S. & Montagner, J.-P. Seismic evidence of flow at the base of the upper mantle. *Geophys. Res. Lett.* **25,** 1995–1998 (1998).
8. Tong, C., Gudmundsson, O. & Kennett, B. L. N. Shear wave splitting in refracted waves returned from the upper mantle transition zone beneath northern Australia. *J. Geophys. Res.* **99,** 15783–15797 (1994).
9. Fouch, M. J. & Fischer, K. M. Mantle anisotropy beneath northwest Pacific subduction zone. *J. Geophys. Res.* **101,** 15987–16002 (1996).
10. Fischer, K. & Wiens, D. The depth distribution of mantle anisotropy beneath the Tonga subduction zone. *Earth Planet. Sci. Lett.* **142,** 253–260 (1996).
11. Montagner, J.-P. & Kennett, B. L. N. How to reconcile body-wave and normal-mode reference Earth models. *Geophys. J. Int.* **125,** 229–248 (1996).
12. Barruol, G. & Hoffmann, R. Upper mantle anisotropy beneath Geoscope stations. *J. Geophys. Res.* **104,** 10757–10773 (1999).
13. Clitheroe, G. & Van der Hilst, R. in *Structure and Evolution of the Australian Continent* (ed. Braun, J. *et al.*) 73–78 (Geodynamics series 26, American Geophysical Union, Washington DC, 1998).
14. Özalaybey, S. & Chen, W. Frequency dependent analysis of SKS/SKKS waveforms observed in Australia: evidence for null birefringence. *Phys. Earth Planet. Inter.* **114,** 197–210 (1999).
15. Silver, P. G. & Chan, W. W. Implications for continental structure and evolution from seismic anisotropy. *Nature* **335,** 34–39 (1988).
16. Wolfe, C. J. & Silver, P. G. Seismic anisotropy of oceanic upper mantle: Shear-wave splitting methodologies and observations. *J. Geophys. Res.* **103,** 749–771 (1998).
17. Kendall, J.-M. & Thomson, C. J. Seismic modelling of subduction zones with inhomogeneity and anisotropy, I: Teleseismic P-wavefront geometry. *Geophys. J. Int.* **112,** 39–66 (1993).
18. Kirby, S. H., Durham, W. B. & Stern, L. A. Mantle phase changes and deep-earthquake faulting in subducting lithosphere. *Science* **252,** 216–225 (1991).
19. Anderson, D. L. Thermally induced phase changes, lateral heterogeneity of the mantle, continental roots and deep slab anomalies. *J. Geophys. Res.* **92,** 13968–13980 (1987).
20. Mainprice, D., Barruol, G. & Ismaïl, W. B. in *Earth's Deep Interior: Mineral Physics and Tomography from the Atomic to the Global Scale* (eds Karato, S., Fortre, A., Masters, T. G. & Stixrude, L.) 237–264 (Geophysical Monographs 117, American Geophysical Union, Washington DC, 2000).
21. Karato, S., Dupas-Bruzek, C. & Rubie, D. Plastic deformation of silicate spinel under the transition-zone conditions of the Earth's mantle. *Nature* **395,** 266–269 (1998).
22. Meade, C. P., Silver, P. G. & Kaneshima, S. Laboratory and seismological observations of lower mantle isotropy. *Geophys. Res. Lett.* **22,** 1293–1296 (1995).
23. Yeganeh-Haeri, A. Synthesis and re-investigation of the elastic properties of single-crystal magnesium silicate perovskite. *Phys. Earth Planet. Inter.* **87,** 111–121 (1994).
24. Oganov, A. R., Brodholt, J. P. & Price, G. D. The elastic constants of $MgSiO_3$ perovskite at pressures and temperatures of the Earth's mantle. *Nature* **411,** 934–937 (2001).
25. Stixrude, L. in *The Core-Mantle Boundary Region* (eds Gurnis, M., Wysession, M., Knittle, E. & Buffett, B.) 83–96 (Geodynamics series 28, American Geophysical Union, Washington DC, 1998).
26. Gaherty, J. B. & Jordan, T. H. Lehmann discontinuity as the base of an anisotropic layer beneath continents. *Science* **268,** 1468–1471 (1995).
27. Kusznir, N. J. Subduction body force stresses and viscosity structure at the 410 km and 660 km phase transitions. *Eos* **81,** 1081 (2000).
28. Ringwood, A. E. Role of the transition zone and 660 km discontinuity in mantle dynamics. *Phys. Earth Planet. Inter.* **86,** 5–24 (1994).
29. Mitrovica, J. X. & Forte, A. M. Radial profile of mantle viscosity: Results from the joint inversion of convection and postglacial rebound observations. *J. Geophys. Res.* **102,** 2751–2769 (1997).
30. Hirose, K., Fei, Y., Ma, Y. & Mao, H.-K. The fate of subducted basaltic crust in the Earth's lower mantle. *Nature* **397,** 53–56 (1999).
31. Widiyantoro, S., Kennett, B. L. N. & Van der Hilst, R. Seismic tomography with P and S data reveals lateral variations in the rigidity of deep slabs. *Earth Planet. Sci. Lett.* **173,** 91–100 (1999).
32. Van der Hilst, R. Complex morphology of subducted lithosphere in the mantle beneath the Tonga trench. *Nature* **374,** 154–157 (1995).

Supplementary Information accompanies the paper on *Nature*'s website (http://www.nature.com).

Acknowledgements

We thank K. Fischer, G. Houseman and M. Casey for comments on the manuscript, and K. Fischer for suggesting alternative models to test.

Competing interests statement

The authors declare that they have no competing financial interests.

Correspondence and requests for materials should be addressed to J.-M.K. (e-mail: m.kendall@earth.leeds.ac.uk).

A basal troodontid from the Early Cretaceous of China

Xing Xu*, Mark A. Norell†, Xiao-lin Wang*, Peter J. Makovicky‡ & Xiao-chun Wu§

* *Institute of Vertebrate Paleontology and Paleoanthropology, Chinese Academy of Sciences, Beijing 100044, China*
† *American Museum of Natural History, Central Park West at 79th Street, New York, New York 10024, USA*
‡ *The Field Museum, 1400 S Lake Shore Drive, Chicago, Illinois 60605, USA*
§ *Canadian Museum of Nature, Station D, Ottawa, Ontario K1P 6P4, Canada*

Troodontid dinosaurs form one of the most avian-like dinosaur groups[1–5]. Their phylogenetic position is hotly debated, and they have been allied with almost all principal coelurosaurian lineages[6–13]. Here we report a basal troodontid dinosaur, *Sinovenator changii* gen. et sp. nov., from the lower Yixian Formation of China. This taxon has several features that are not found in more derived troodontids, but that occur in dromaeosaurids and avialans. The discovery of *Sinovenator* and the examination of character distributions along the maniraptoran lineage indicate that principal structural modifications toward avians were acquired in the early stages of maniraptoran evolution.

Theropoda Marsh, 1881
Maniraptora Gauthier, 1986
Troodontidae Gilmore, 1924
Sinovenator changii gen. et sp. nov.

Holotype. IVPP (Institute of Vertebrate Paleontology and Paleoanthropology, Beijing) V 12615, a disarticulated partial skull and skeleton.

Referred specimen. IVPP V12583, an incomplete, articulated postcranial skeleton.

Etymology. '*Sinae*', Latin referring to China, plus '*Venator*', Latin for hunter. The specific name honours Meeman Chang of the IVPP for her significant role in the study of the Jehol fauna.

Locality and horizon. Lujiatun and Yanzigou, Shanyuan, western Liaoning, China; lowest part of Yixian Formation, older than 128 Myr (ref. 14; Hauterivian?); associated vertebrate fossils include the ceratopsian *Psittacosaurus*, the primitive ornithischian *Jeholosaurus*[15], and the primitive mammal *Repenomamus*[16].

Diagnosis. A troodontid with the following derived characters: straight and vertical anterior margin of antorbital fenestra; frontal with a vertical lamina bordering the lacrimal; surangular T-shaped

